Article

Monte Carlo Study of Imaging Plate Response to Laser-Driven Aluminum Ion Beams

Junho Won [1,2], Jaehyeon Song [1,2], Sasi Palaniyappan [3], Donald Cort Gautier [3], Wonhee Jeong [1], Juan Carlos Fernández [3] and Woosuk Bang [1,2,*]

1   Department of Physics and Photon Science, Gwangju Institute of Science and Technology (GIST), Gwangju 61005, Korea; wonder112@gist.ac.kr (J.W.); songjh8975@gist.ac.kr (J.S.); wonhee1990@gist.ac.kr (W.J.)
2   Center for Relativistic Laser Science, Institute for Basic Science, Gwangju 61005, Korea
3   Los Alamos National Laboratory, Los Alamos, NM 87545, USA; sasi@lanl.gov (S.P.); gautier@lanl.gov (D.C.G.); juanc@lanl.gov (J.C.F.)
*   Correspondence: wbang@gist.ac.kr

Abstract: We measured the response of BAS-TR imaging plate (IP) to energetic aluminum ions up to 222 MeV, and compared it with predictions from a Monte Carlo simulation code using two different IP response models. Energetic aluminum ions were produced with an intense laser pulse, and the response was evaluated from cross-calibration between CR-39 track detector and IP energy spectrometer. For the first time, we obtained the response function of the BAS-TR IP for aluminum ions with a kinetic energy as high as 222 MeV. On close examination of the two IP response models, we confirm that the exponential model fits our experimental data better. Moreover, we find that the IP sensitivity in the exponential model is nearly constant in this energy range, suggesting that the response function can be determined even with little experimental data.

Keywords: Monte Carlo simulation; laser-driven ion acceleration; imaging plate

1. Introduction

An imaging plate (IP) is a film-like image sensor that records the incident radiation flux on a thin sheet called a phosphor layer. It is known to be sensitive to energetic charged particles, X-rays, and gamma rays [1–4]. Since IPs were developed by Fuji film Co. in the early 1980s, they have been widely used in nuclear science and in medicine. While an IP is a passive detector and cannot be used in high repetition rate experiments, IPs have several advantages over other particle detectors: (1) immunity to electromagnetic pulse (EMP), (2) high dynamic range (4–5 orders of magnitude), (3) high spatial resolution (resolving to as low as 10 µm), and (4) reusability (signals of IPs can be erased with white light) [1,5–7]. For radiation detection, Biological Analysis System (BAS) IP types are commonly used [8]. Specifically, BAS-MS, SR, and TR IPs were primarily designed for high sensitivity, high resolution, and detection of beta particles from tritium, respectively [9,10].

BAS IPs typically consist of three or four layers with various thicknesses: a protective layer, a phosphor layer, a support layer, and a magnetic layer. The BAS-TR IP has no protective layer [11], and the lack of a protective layer makes BAS-TR IP particularly well suited to measure heavy ions with short ranges within matter. Incoming ions deposit kinetic energy in the 50 µm thick phosphor layer [11]. Beneath the 250 µm thick support layer, there is a 160 µm thick magnetic layer which allows for magnetic attachment of the IP to the scanner [12].

When an IP is exposed to radiation, the electrons of Eu^{2+} in the phosphor layer are ionized and trapped in FBr or FI sites forming metastable states. The lifetimes of the metastable states range from 10 min to several days. When a scanner irradiates the phosphor layer with 2 eV photons from a laser diode, the electrons in the metastable state

are re-excited and recombine with Eu^{3+} and emit 3 eV photons. That emission is known as the photostimulated luminescence (PSL). To use an IP as a quantitative radiation detector, it is necessary to calibrate the PSL relative to the spectral intensity of radiation. For ions, the spectral response function of an IP is measured in units of PSL per incident ion of a given energy. This must be done for each type of radiation and IP and scanner combination, because each combination has in general different responses [5,7,13–16].

Researchers have measured the response of IPs to various radiation types such as electrons [5,7,13,17–21], protons [12,14,22–24], and X-ray [16,25] for a wide energy range. The measurement of IP responses to energetic heavy ion beams, however, is more challenging because it is difficult to produce heavy ion beams with sufficient particle fluence for IP calibration at a range of energies in a reasonably short time. For this reason, the published studies of IP response to ions are limited to a few types of heavier elements such as deuterium [23,26], helium [16,23], carbon [6], and titanium [27].

Since Hidding et al. [28] proposed a linear model predicting the response of IP, some researchers have calculated the IP response by calculating stopping powers using Monte Carlo simulation codes. Bonnet et al. designed an exponential model and calibrated the IP response to protons, electrons, photons, and ^{4}He ions, using Geant4 [14,16,29]. Recently, Rabhi et al. reported on the responses of BAS-MS, SR, and TR for 1–200 MeV protons [12] and for 40–180 MeV electrons [21] using Geant4. Singh et al. used FLUKA to calibrate the responses of BAS-MS and SR to 150 keV–1.75 MeV electrons [5].

In this paper, we report on the IP response to aluminum (Al) ions for the first time, with an incident kinetic energy as high as 222 MeV. We have used an Al ion beam driven by an intense laser pulse as the ion source, and detected these ions using BAS-TR IPs for the measurements. We compare both the linear model and the exponential model with our experimental results for Al ions. In our study, we have used the Monte Carlo simulation code SRIM [30] to calculate the stopping powers of a BAS-TR IP for Al ions because SRIM is known to represent the available experimental data well [31,32]. We show that the response function calculations using stopping power from SRIM code agree very well with our experimental data for Al ions up to 222 MeV. We find that the IP sensitivity remains nearly constant for all the incident Al ion energy in the exponential model, which suggests that the IP response function can be calculated for the entire energy range of the ion beams using just a few experimental data points.

2. Experimental Setup

The experiments were performed on the Trident laser facility at Los Alamos National Laboratory (LANL) [33,34]. Figure 1 shows the schematic layout of the experimental setup. 80 J, 650 fs, 1054 nm laser pulses were focused using an f/3 off-axis parabola, and irradiated 110 nm thick aluminum foils with a peak laser intensity of about 2×10^{20} W/cm^2 [33]. The laser-driven Al ion beams diverged with a 20° cone half-angle [35,36]. The ions fly into a high resolution and high dispersion Thomson Parabola Spectrometer (TPS) [33,37], which measures an energy spectrum of the ions separately depending on their charge to mass (Z/A) ratio. The TPS symmetry axis is aligned with the ion propagation direction, and the ion flux into the TPS is limited by a pinhole aperture along that axis. Over a portion of the ion flight within the TPS, strong electric (E) and magnetic (B) fields parallel to each other and normal to the symmetry axis deflects ions depending on their Z/A and kinetic energy (E_{ion}). After a drift distance within the TPS, they arrive at the detector plane laid normal to the axis. The Z/A and E_{ion} are given by their location on this plane [33,37]. Specifically, the TPS disperses a given Z/A on the detector plane along a narrow (as defined by the pinhole) parabolic curve in the $\hat{x}$ (horizontal, B-field deflection) and $\hat{y}$ (vertical, E-field deflection) directions originating at the intersection with the symmetry axis according to E_{ion}. The origin (= zero point in Figure 2) corresponds to an infinite E_{ion}, and X-rays or neutral particles are recorded as well. The TPS uses 10 cm long magnets producing 0.82 T and 50 cm long electrodes that can be charged up to 15 kV potential., enabling high energy resolutions of $\Delta E/E < 5\%$ at 100 MeV/nucleon [33,37]. The IP used in the

TPS was covered with an 18 μm thick Al filter in order to eliminate background noise originating from scattered laser lights, low energy protons (<1 MeV), low energy electrons (<50 keV), and soft X-rays [33]. Incident Al ions with kinetic energy greater than 50 MeV penetrated through the filter and reached the IP surface. For counting the absolute number of aluminum ions, strip-shaped CR-39 track detectors with a width of a few mm were placed on the IP surface [33].
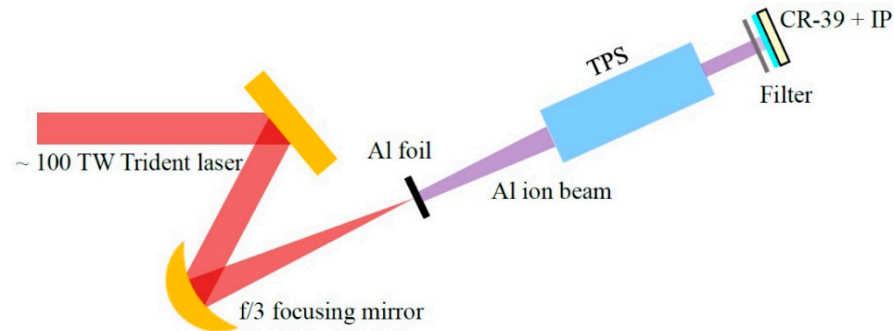

Figure 1. Schematic layout of the experimental setup. An intense laser pulse produces energetic Al ions, which are detected using CR-39 and IP.
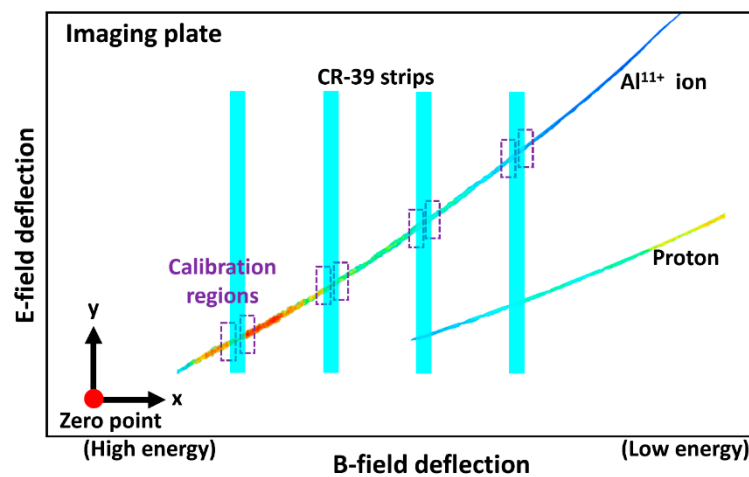

Figure 2. Schematic layout of the CR-39 strips on the IP. The laser-driven Al ions that are deflected inside the TPS leave traces on the CR-39 strips and BAS-TR IP. Calibration regions are marked as purple rectangles in the figure. At each boundary of the calibration region, PSL/ion values are measured by comparing the number of tracks on the CR-39 and the amount of PSL from the IP.

It is known that the IP response does not depend on the charge state of the incident ions [6,23,38,39]. This is because the incident ions quickly arrive at an equilibrium charge state as soon as they enter the target surface. This characteristic is assumed by Freeman et al. [23], and is confirmed by Doria et al. [6] and J. Strehlow et al. [27] in experiments using multiply charged carbon ions and titanium ions, respectively. Therefore, we do not need to specify the charge state of Al ions incident on the BAS-TR IP in our SRIM simulations.

3. Measurement of PSL/Ion

After exposing the calibration region of an IP to energetic aluminum ions, PSL is measured experimentally using a scanner. In this experiment, we scanned each IP 5 min after exposing it to an ion beam. The BAS-TR IP was scanned by a commercial scanner (Fujifilm Typhoon FLA-7000). The input light in the scanner is converted to electronic signals, which are stored in a PC as quantum level (QL) pixel-resolved image data. Since

QL encodes a logarithmic response, a conversion is required to extract the linear PSL data. The conversion formula from a QL value to a PSL value is [6]

$$\text{PSL} = \left(\frac{R}{100}\right)^2 \times \frac{4000}{S} \times 10^{L \times \left(\frac{QL}{2^G - 1} - \frac{1}{2}\right)},\tag{1}$$

where $R = 25$ μm is the resolution of the scanner, S is the scanner sensitivity setting selected from 1000 to 10,000, $L = 5$ is the latitude parameter which relates to the dynamic range of the scanner, and $G = 16$ is the gradation parameter for 16-bit image data.

The PSL/ion value was obtained from cross-calibration between the amount of PSL scanned in the Al^{11+} trajectory adjacent to a CR-39 strip and the number of ions counted in the pits of the strip. This calibration method assumes that there is no sharp discontinuity in the areal density of Al^{11+} ions on the track nearby the edges of the CR-39 bars. These calibration regions are illustrated in Figure 2, which shows the schematic layout of the CR-39 strips on the BAS-TR IP. E_{ion} is readily obtained from the TPS data based on the analytic expressions for the ion deflection at the detector plane. The x-direction deflection (due to the known E) is used to obtain E_{ion}/q, where q is the ion charge. That value is plugged into the equation for the y-direction deflection (due to the known B) to obtain Z/A. Since we know A (Al), we obtain q and E_{ion}. Thus, PSL/ion value for Al^{11+} ions can be obtained for the E_{ion} of Al^{+11} ions corresponding to each edge of the CR-39 strip along the track.

4. Fading Effect

As time elapses after activation, some of the electrons in the metastable states spontaneously decay to the Eu^{3+} state and emit PSL. This phenomenon is called the fading effect, and the resulting PSL loss when the IP is scanned subsequently should be taken into account in the analysis. Several studies have measured fading curves for electrons [13,17], protons [14], X-rays [5,7,15,26], and γ-rays [14]. Although the radiation sources used in fading measurements are different in each experiment, fading curves are not very sensitive to the type and energy of radiation. Bonnet et al. find that fading signals are nearly independent of the radiation type with less than 10% differences between photons and protons [14]. Ohuchi et al. also report that the fading effect is similar for electrons and for protons regardless of their kinetic energies [40]. The known parameters contributing to fading effect are ambient temperature and scanner type [7]. Although the fading effect becomes bigger as the ambient temperature increases, its change can be considered negligible for a small temperature fluctuation [7].

Zeil et al. [13] report different fading behaviors between their data measured by BAS-1800II and the data of Tanaka et al. [17] measured by BAS-5000. Their findings suggest that PSL signals measured using different scanners can be quite different [13]. Ohuchi et al. also compared BAS-1000 and BAS-5000 and observed that fading of BAS-5000 is larger than that of BAS-1000 [40]. Therefore, we need to apply a fading model benchmarked using the same IP with the same scanner. Bonnet et al. [14] and Boutoux et al. [7] have used the same FLA-7000 scanner as in our measurements, and their fading functions are quite comparable each other. They have both used two exponential functions to fit their data, and we have adopted the fading function of Boutoux et al. as shown below [7].

$$f(t) = 0.535\, e^{\frac{-t}{\tau_1}} + 0.465\, e^{\frac{-t}{\tau_2}},\tag{2}$$

where $\tau_1 = 23.812$ (min), $\tau_2 = 3837.2$ (min). In our experiment, fading loss is expected to be about 10% at $t = 5$ (min), and thus the experimentally measured PSL values have been scaled upwards to the values that would have been measured at time zero.

5. Calculation of PSL/Ion from SRIM Data

There are two models commonly used to predict the amount of PSL from a given radiation. Hidding et al. [28] propose a linear model assuming that the yield of PSL is proportional to the total deposited energy in the sensitive layer of an IP.

$$R(E_{ion}) = \alpha E_{dep}(E_{ion}), \tag{3}$$

where $R(E_{ion})$ is the IP response for ions with incident kinetic energy of E_{ion} and α is the IP sensitivity. The IP sensitivity varies depending on the type of radiation and IPs. It also depends on the waiting time before scanning because of the fading loss. The total deposited energy, $E_{dep}(E_{ion})$, is obtained from the integral of the ion-stopping power $S(z)$ at depth z. In the phosphoric layer of the IP,

$$E_{dep} = \int_0^W S(z) dz, \tag{4}$$

where $S(z) = -dE_{ion}/dz$ and W is the thickness of the layer.

The incident ion loses its kinetic energy to electrons in the target by ion-electron collisions resulting from Coulomb interaction and to target nuclei by ion-nucleon collisions (called recoil process). In our SRIM simulations, the predominant process is Coulomb interaction, and the recoil energy contributes only $\sim 10^{-4}$ to the entire collision process. The cross-section for ion-electron interaction is inversely proportional to the square of the approaching speed of the ion.

Bonnet et al. [14] proposed a model for the deposited energy that accounts for the optical thickness of the IP to the PSL radiation by weighting the stopping power by an exponential decay term, i.e.,

$$E_{dep} = \int_0^W S(z) e^{-\frac{z}{L}} dz, \tag{5}$$

where L is the absorption length of PSL photons within the phosphor layer of the IP [14], which is 44 ± 4 μm for BAS-TR IPs [16]. A large L implies that the PSL photons pass through the phosphor layer easily without being absorbed within it [16], and thus a negligible correction. However, $L = 44$ μm indicates that a significant amount of PSL is absorbed since the thickness phosphor layer of BAS-TR IP is 50 μm. Equation (4) can also be interpreted as a special case when the absorption length is infinity and there is no absorption [14]. We refer IP models proposed by Hidding et al. and Bonnet et al. as the linear model and the exponential model, respectively, in the following analysis.

To obtain the stopping power for Al beams, we use the Monte Carlo simulation code SRIM which calculates the stopping and range of ions in matter using a quantum mechanical treatment of ion-atom collision [30]. Each simulation is performed with 10,000 incidences and calculated stopping power and other values are averaged over the 10,000 incidences. We calculate E_{dep} using two different methods (1) by using the averaged $S(z)$ obtained directly from SRIM, and (2) by calculating the absorbed energy and $e^{-\frac{z}{L}}$ at each step from individual incidence then averaging E_{dep} over 10,000 incidences. SRIM divides the target depth into 100 steps in the first method, and about 700 uniform steps in the second method, which determines the simulation resolution. Although the second method has seven times higher target depth resolution in computing the total deposited energy in the phosphor layer, the discrepancy in the deposited energy calculations by each method is found to be only 0.01–0.1%.

In the linear model, we have calculated $S(z)$ using the first method for simplicity. In the exponential model, we have used the second method to calculate $S(z)$ since more steps can potentially reduce errors involved in calculating the weighting factor $e^{-\frac{z}{L}}$. For each IP model, the total deposited energy is calculated as follows

$$E_{dep} = \sum_{i=1}^l \left[\frac{S(z_i) + S(z_{i+1})}{2}\right](z_{i+1} - z_i), \quad \text{(Linear model)} \tag{6}$$

$$E_{dep} = \sum_{i=1}^{l} \left(-\frac{dE}{dz}\right) e^{-\frac{1}{L}\left(\frac{z_{i+1}+z_i}{2}\right)} dz = \sum_{i=1}^{l} -(E_{i+1} - E_i) e^{-\frac{1}{L}\left(\frac{z_{i+1}+z_i}{2}\right)},$$

(Exponential model)

(7)

where z_i is the target depth (the distance that an Al ion passes through the target), $S(z_i)$ is the stopping power of target at depth z_i, E_i is the kinetic energy of the Al ion at z_i, and l is the total number of steps ($l = 100$ or $l = 700$). In the linear model, the area under the curve of stopping power as a function of target depth represents the deposited energy. We use the average of two stopping power values in each interval, and estimate the target depth of each thin layer as $\frac{z_{i+1}+z_i}{2}$ in the exponential model.

The average stopping powers of phosphor layer for mono-energetic Al ions are shown as functions of the target depth in Figure 3 for 130 MeV Al ions (dashed green line) and for 200 MeV Al ions (dot dashed blue line). The 50 μm thick phosphor layer of BAS-TR IP is thick enough to stop all Al ions with $E_{ion} \leq 130$ MeV, so the entire E_{ion} is absorbed within the phosphor layer. For 200 MeV Al ions, on the other hand, the stopping power gradually increases as the ions lose their kinetic energy, but the ions penetrate through the phosphor layer with significant energy remaining.
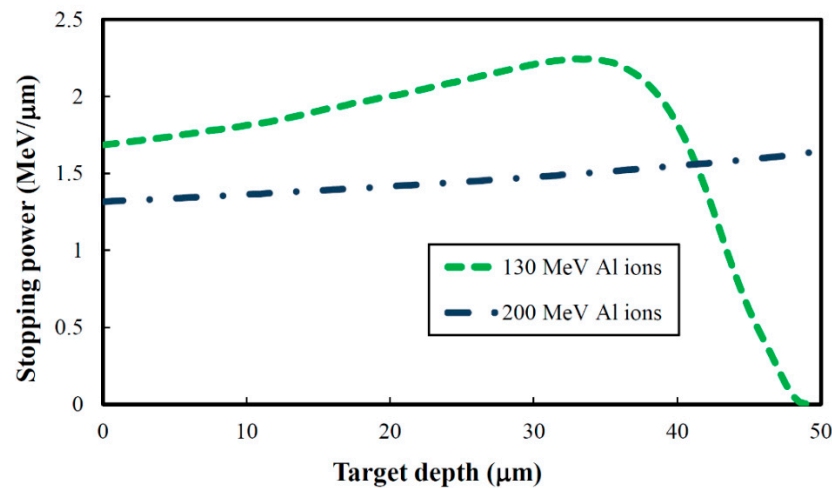

Figure 3. Stopping power of the 50 μm thick phosphor layer of a BAS-TR IP for 130 MeV and 200 MeV Al ions as functions of the target depth. The area under the curve represents the deposited energy in the phosphor layer.

Figure 4a shows the IP response, $R(E_{ion})$, as a function of Al ion energy for our setup. Solid black circles indicate the experimental measurements of PSL/ion data. Error bars are estimated to be ±15%, which account for the decay uncertainty from the fading effect during the time gap (5 min), PSL stimulated by diode laser during scanning, inaccurate calibration of the PMT, and IP surface quality (roughness) [6]. The dashed black line represents the IP response calculated using the linear model, and the solid red line shows the IP response calculated using the exponential model with $L = 44$ μm. The calculated IP responses with ± one standard deviation (±4 μm) of L are shown when $L = 48$ μm (dashed red line) and $L = 40$ μm (dot dashed red line). In both models, the total deposited energy increases as the kinetic energy of Al ion increases from 50 MeV to 140 MeV, but it decreases beyond 140 MeV. The IP response from the exponential model increases more gradually and it fits the experimental data better.

As is described in the experimental setup section, there was an 18 μm thick filter in front of our BAS-TR IP, and only ions with sufficient kinetic energy (larger than 50 MeV) arrived at the IP front surface. Since filter arrangements can differ for each experiment, beyond the computation of our specific filter conditions, we aim to produce a response model applicable to arbitrary filter arrangements. We start with the computed incident ion energy on the front phosphor layer surface obtained by subtracting the energy loss in the 18 μm thick filter from the incoming E_{ion} measured with the TPS. We computed

Al ion energy loss in the filter with SRIM. Figure 4b shows energy loss from an 18 μm thick Al filter as a function of the incident Al ion energy. The dashed green line indicates the kinetic energy loss of energetic Al ions. The solid blue line shows the incident kinetic energy of Al ions on the phosphor layer after penetrating through the filter as a function of the initial Al ion energy before the filter. Figure 4c shows the IP response as a function of the incident Al ion energy on the phosphor layer. The horizontal axis corresponds to the kinetic energy of the incident Al ion after penetrating through the filter, which is calculated in Figure 4b. Solid black circles represent the experimentally measured IP responses, and the dashed black line indicates the IP response calculated using the linear model. The solid red line represents the IP response calculated using the exponential model with an absorption length of $L = 44$ μm. For both the linear and the exponential model, we have used the method of least squares and determined the IP sensitivity, α, from Figure 4c. The IP responses with $\pm$ one standard deviation of the absorption length are also plotted in the same figure for $L = 48$ μm (dashed red line) and for $L = 40$ μm (dot dashed red line).
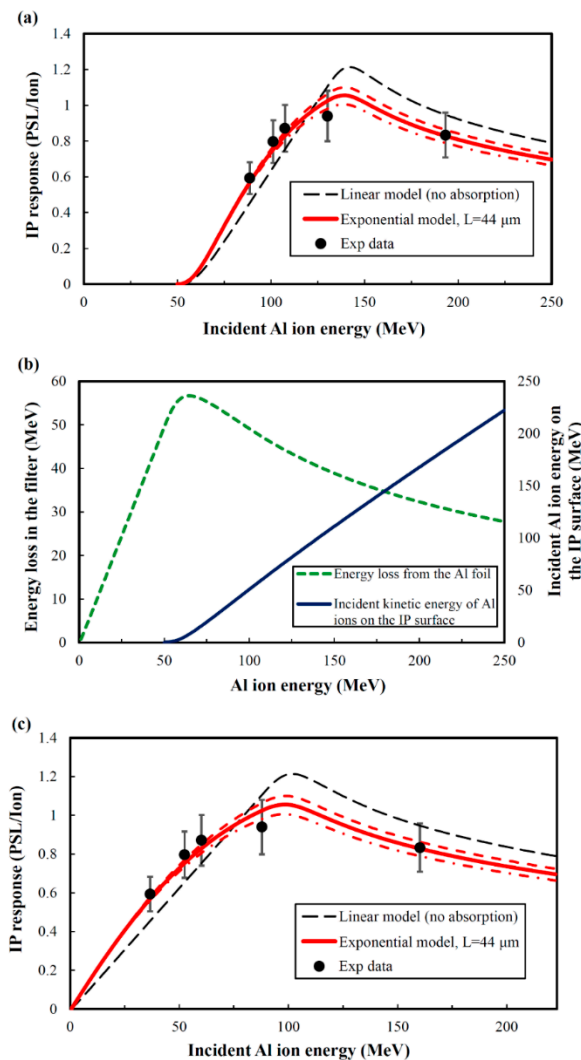

Figure 4. (**a**) IP response of BAS-TR IP is shown as a function of incoming Al ion energy before the filter. (**b**) Energy loss in the filter is shown as a function of Al ion energy (dashed green line). The incident kinetic energy of Al ions on the phosphor layer after penetrating through the filter is also shown as a function of Al ion energy (solid blue line). (**c**) IP response of BAS-TR IP is shown as a function of the incident Al ion energy on the phosphor layer.

6. IP Sensitivity

We examined how IP sensitivities at different incident Al ion energy deviate from the IP sensitivity obtained by least squares method in each model. Figure 5 shows the IP sensitivities as functions of the incident Al ion energy for both the linear model and the exponential model. The IP sensitivities calculated using the exponential model are shown as hollow red circles, and those calculated using the linear model are plotted as hollow black circles. These values are derived from experimentally measured IP responses and the calculated deposited energy from the incident Al ions using each model. In Figure 5, the IP sensitivity fluctuation in the exponential model is less than that in the linear model. The IP sensitivity is nearly constant at $\alpha_{exp} = 0.019$ in the exponential model with a standard deviation of 5% of α_{exp}. In the linear model, the IP sensitivity is $\alpha_{lin} = 0.013$ with a standard deviation of 21% of α_{lin}. This suggests that the exponential model describes the IP response better.
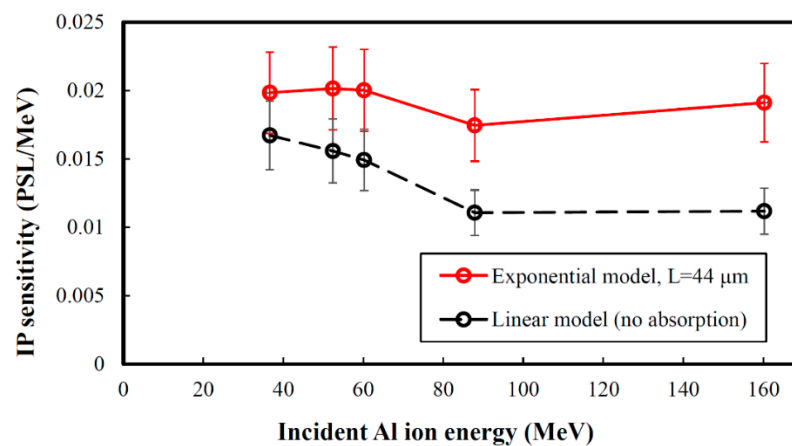

Figure 5. Sensitivity of BAS-TR IP is shown as a function of the incident Al ion energy on the IP surface.

Since the IP sensitivity in the exponential model remains nearly unchanged regardless of the incident kinetic energy of Al ions in Figure 5, we can treat α_{exp} as a constant value in Equation (3) and determine the IP response function by multiplying the deposited energy function calculated from the Monte Carlo simulations. This implies that the IP response function can be calculated even with little experimental data.

The overall sensitivity of BAS-TR IP to Al ions is found to be much smaller than the known sensitivity of IPs to electrons, protons, and alpha particles. This is consistent with the findings reported by Freeman et al. [23] and Bonnet et al. [16] for alpha particles. Bonnet et al. report that the IP sensitivity to ^{4}He ions is about 10 times smaller than the IP sensitivity to protons with BAS-MS and BAS-SR IPs and around five times smaller than the IP sensitivity to protons with BAS-TR IP [16]. Bonnet et al. explain this using a quenching effect. According to their study, the IP sensitivity depends on both the type of incident ions and the stopping power of IPs for those ions [16,23].

In our experiment, a similar quenching effect is also observed. The measured sensitivity of BAS-TR IP to Al ions is about 13 times less than the known IP sensitivity to protons, and it is about half of the known IP sensitivity to ^{4}He [16]. As shown in Figure 5, IP sensitivities decrease with increasing incident Al ion energy. This decrease is larger in the linear model than in the exponential model. The large variations of the IP sensitivities in the linear model seem to be caused by the quenching effect, which results in large discrepancy with the experimental IP response data. In comparison, the exponential model has smaller variations of the IP sensitivity and agrees well with the experimental data. The exponential factor in Equation (5) offsets the IP sensitivity decline coming from the stopping power increase of Al ions.

7. Conclusions

For the first time, we measured the response of BAS-TR IP to Al ions up to 222 MeV. The PSL/ion values were measured experimentally using CR-39 track detectors and an ion energy spectrometer, and the measurements were compared with calculated deposited energy. We propose a technique to calculate deposited energy in the phosphor layer using stopping power calculations from SRIM code. The response function taking the absorption length into account is in very good agreement with the experimental data. We find that the exponential model predicting the response of an IP fits the experimental data better. The IP sensitivity is nearly constant regardless of the incident energies of aluminum ion beams, suggesting that the IP response function can be calculated even with little experimental data. Our simulations and analysis provide a straightforward method using stopping power calculations to find the response function of an imaging plate to other energetic heavy ion beams.

Author Contributions: Conceptualization, W.B.; methodology, S.P., D.C.G., and J.C.F.; formal analysis, J.W., J.S., and W.J.; writing—original draft preparation, J.W., W.B.; writing—review and editing, J.W., W.B.; visualization, J.W.; supervision, W.B.; project administration, W.B.; funding acquisition, J.C.F. and W.B. All authors have read and agreed to the published version of the manuscript.

References

1. Amemiya, Y.; Miyahara, J. Imaging plate illuminates many fields. *Nature* **1988**, *336*, 89. [CrossRef] [PubMed]
2. Amemiya, Y.; Wakabayashi, K.; Tanaka, H.; Ueno, Y.; Miyahara, J. Laser-stimulated luminescence used to measure X-ray diffraction of a contracting striated muscle. *Science* **1987**, *237*, 164. [CrossRef] [PubMed]
3. Cipiccia, S.; Islam, M.R.; Ersfeld, B.; Shanks, R.P.; Brunetti, E.; Vieux, G.; Yang, X.; Issac, R.C.; Wiggins, S.M.; Welsh, G.H.; et al. Gamma-rays from harmonically resonant betatron oscillations in a plasma wake. *Nat. Phys.* **2011**, *7*, 867. [CrossRef]
4. Ta Phuoc, K.; Corde, S.; Thaury, C.; Malka, V.; Tafzi, A.; Goddet, J.P.; Shah, R.C.; Sebban, S.; Rousse, A. All-optical Compton gamma-ray source. *Nat. Photonics* **2012**, *6*, 308. [CrossRef]
5. Singh, S.; Slavicek, T.; Hodak, R.; Versaci, R.; Pridal, P.; Kumar, D. Absolute calibration of imaging plate detectors for electron kinetic energies between 150 keV and 1.75 MeV. *Rev. Sci. Instrum.* **2017**, *88*, 075105. [CrossRef] [PubMed]
6. Doria, D.; Kar, S.; Ahmed, H.; Alejo, A.; Fernandez, J.; Cerchez, M.; Gray, R.J.; Hanton, F.; MacLellan, D.A.; McKenna, P.; et al. Calibration of BAS-TR image plate response to high energy (3-300 MeV) carbon ions. *Rev. Sci. Instrum.* **2015**, *86*, 123302. [CrossRef]
7. Boutoux, G.; Rabhi, N.; Batani, D.; Binet, A.; Ducret, J.E.; Jakubowska, K.; Nègre, J.P.; Reverdin, C.; Thfoin, I. Study of imaging plate detector sensitivity to 5-18 MeV electrons. *Rev. Sci. Instrum.* **2015**, *86*, 113304. [CrossRef]
8. Boutoux, G.; Batani, D.; Burgy, F.; Ducret, J.E.; Forestier-Colleoni, P.; Hulin, S.; Rabhi, N.; Duval, A.; Lecherbourg, L.; Reverdin, C.; et al. Validation of modelled imaging plates sensitivity to 1-100 keV X-rays and spatial resolution characterisation for diagnostics for the "PETawatt Aquitaine Laser". *Rev. Sci. Instrum.* **2016**, *87*, 043108. [CrossRef]
9. Schlenvoigt, H.P.; Haupt, K.; Debus, A.; Budde, F.; Jäckel, O.; Pfotenhauer, S.; Schwoerer, H.; Rohwer, E.; Gallacher, J.G.; Brunetti, E.; et al. A compact synchrotron radiation source driven by a laser-plasma wakefield accelerator. *Nat. Phys.* **2007**, *4*, 130. [CrossRef]
10. Yu, C.; Qi, R.; Wang, W.; Liu, J.; Li, W.; Wang, C.; Zhang, Z.; Liu, J.; Qin, Z.; Fang, M.; et al. Ultrahigh brilliance quasi-monochromatic MeV γ-rays based on self-synchronized all-optical Compton scattering. *Sci. Rep.* **2016**, *6*, 29518. [CrossRef]

11. Ingenito, F.; Andreoli, P.; Batani, D.; Boutoux, G.; Cipriani, M.; Consoli, F.; Cristofari, G.; Curcio, A.; Angelis, R.D.; Giorgio, G.D.; et al. Comparative calibration of IP scanning equipment. *Comp. Calibration Ip Scanning Equip. J. Instrum.* **2016**, *11*, C05012. [CrossRef]

12. Rabhi, N.; Batani, D.; Boutoux, G.; Ducret, J.-E.; Jakubowska, K.; Lantuejoul-Thfoin, I.; Nauraye, C.; Patriarca, A.; Saïd, A.; Semsoum, A.; et al. Calibration of imaging plate detectors to mono-energetic protons in the range 1-200 MeV. *Rev. Sci. Instrum.* **2017**, *88*, 113301. [CrossRef] [PubMed]

13. Zeil, K.; Kraft, S.D.; Jochmann, A.; Kroll, F.; Jahr, W.; Schramm, U.; Karsch, L.; Pawelke, J.; Hidding, B.; Pretzler, G. Absolute response of Fuji imaging plate detectors to picosecond-electron bunches. *Rev. Sci. Instrum.* **2010**, *81*, 013307. [CrossRef] [PubMed]

14. Bonnet, T.; Comet, M.; Denis-Petit, D.; Gobet, F.; Hannachi, F.; Tarisien, M.; Versteegen, M.; Aleonard, M.M. Response functions of Fuji imaging plates to monoenergetic protons in the energy range 0.6–3.2 MeV. *Rev. Sci. Instrum.* **2013**, *84*, 013508. [CrossRef]

15. Maddox, B.R.; Park, H.S.; Remington, B.A.; Izumi, N.; Chen, S.; Chen, C.; Kimminau, G.; Ali, Z.; Haugh, M.J.; Ma, Q. High-energy X-ray backlighter spectrum measurements using calibrated image plates. *Rev. Sci. Instrum.* **2011**, *82*, 023111. [CrossRef]

16. Bonnet, T.; Comet, M.; Denis-Petit, D.; Gobet, F.; Hannachi, F.; Tarisien, M.; Versteegen, M.; Aléonard, M.M. Response functions of imaging plates to photons, electrons and 4He particles. *Rev. Sci. Instrum.* **2013**, *84*, 103510. [CrossRef]

17. Tanaka, K.A.; Yabuuchi, T.; Sato, T.; Kodama, R.; Kitagawa, Y.; Takahashi, T.; Ikeda, T.; Honda, Y.; Okuda, S. Calibration of imaging plate for high energy electron spectrometer. *Rev. Sci. Instrum.* **2005**, *76*, 013507. [CrossRef]

18. Chen, H.; Back, N.L.; Bartal, T.; Beg, F.N.; Eder, D.C.; Link, A.J.; MacPhee, A.G.; Ping, Y.; Song, P.M.; Throop, A.; et al. Absolute calibration of image plates for electrons at energy between 100keV and 4MeV. *Rev. Sci. Instrum.* **2008**, *79*, 033301. [CrossRef]

19. Nakanii, N.; Kondo, K.; Yabuuchi, T.; Tsuji, K.; Tanaka, K.A.; Suzuki, S.; Asaka, T.; Yanagida, K.; Hanaki, H.; Kobayashi, T.; et al. Absolute calibration of imaging plate for GeV electrons. *Rev. Sci. Instrum.* **2008**, *79*, 066102. [CrossRef]

20. Taniyama, A.; Shindo, D.; Oikawa, T. Sensitivity and Fading Characteristics of the 25 μm Pixel Size Imaging Plate for Transmission Electron Microscopes. *J. Electron Microsc.* **1996**, *45*, 232–235. [CrossRef]

21. Rabhi, N.; Bohacek, K.; Batani, D.; Boutoux, G.; Ducret, J.E.; Guillaume, E.; Jakubowska, K.; Thaury, C.; Thfoin, I. Calibration of imaging plates to electrons between 40 and 180 MeV. *Rev. Sci. Instrum.* **2016**, *87*, 053306. [CrossRef] [PubMed]

22. Choi, I.W.; Kim, C.M.; Sung, J.H.; Kim, I.J.; Yu, T.J.; Lee, S.K.; Jin, Y.Y.; Pae, K.H.; Hafz, N.; Lee, J. Absolute calibration of a time-of-flight spectrometer and imaging plate for the characterization of laser-accelerated protons. *Meas. Sci. Technol.* **2009**, *20*, 115112. [CrossRef]

23. Freeman, C.G.; Fiksel, G.; Stoeckl, C.; Sinenian, N.; Canfield, M.J.; Graeper, G.B.; Lombardo, A.T.; Stillman, C.R.; Padalino, S.J.; Mileham, C.; et al. Calibration of a Thomson parabola ion spectrometer and Fujifilm imaging plate detectors for protons, deuterons, and alpha particles. *Rev. Sci. Instrum.* **2011**, *82*, 073301. [CrossRef] [PubMed]

24. Mančić, A.; Fuchs, J.; Antici, P.; Gaillard, S.A.; Audebert, P. Absolute calibration of photostimulable image plate detectors used as (0.5–20MeV) high-energy proton detectors. *Rev. Sci. Instrum.* **2008**, *79*, 073301. [CrossRef]

25. Dong, Y.; Zhang, Z.; Xu, M.; Du, Y.; Zhang, C.; Dong, X.; He, Y.; Tan, J.; Zhang, Y.; Zhu, C.; et al. Absolute X-ray calibration of an Amersham imaging plate scanner. *Rev. Sci. Instrum.* **2020**, *91*, 033105. [CrossRef]

26. Alejo, A.; Kar, S.; Ahmed, H.; Krygier, A.G.; Doria, D.; Clarke, R.; Fernandez, J.; Freeman, R.R.; Fuchs, J.; Green, A.; et al. Characterisation of deuterium spectra from laser driven multi-species sources by employing differentially filtered image plate detectors in Thomson spectrometers. *Rev. Sci. Instrum.* **2014**, *85*, 093303. [CrossRef]

27. Strehlow, J.; Forestier-Colleoni, P.; McGuffey, C.; Bailly-Grandvaux, M.; Daykin, T.S.; McCary, E.; Peebles, J.; Revet, G.; Zhang, S.; Ditmire, T.; et al. The response function of Fujifilm BAS-TR imaging plates to laser-accelerated titanium ions. *Rev. Sci. Instrum.* **2019**, *90*, 083302. [CrossRef]

28. Hidding, B.; Pretzler, G.; Clever, M.; Brandl, F.; Zamponi, F.; Lübcke, A.; Kämpfer, T.; Uschmann, I.; Förster, E.; Schramm, U.; et al. Novel method for characterizing relativistic electron beams in a harsh laser-plasma environment. *Rev. Sci. Instrum.* **2007**, *78*, 083301. [CrossRef]

29. Bonnet, T.; Comet, M.; Denis-Petit, D.; Gobet, F.; Hannachi, F.; Tarisien, M.; Versteegen, M. Two parameter model of Fuji imaging plate response function to protons. In Proceedings of the SPIE Optics + Optoelectronics, Prague, Czech Republic, 9 May 2013; p. 7. [CrossRef]

30. Ziegler, J.F.; Ziegler, M.D.; Biersack, J.P. SRIM—The stopping and range of ions in matter. *Nucl. Instrum. Methods Phys. Res. Sect. B Beam Interact. Mater. At.* **2010**, *268*, 1818–1823. [CrossRef]

31. Paul, H.; Sánchez-Parcerisa, D. A critical overview of recent stopping power programs for positive ions in solid elements. *Nucl. Instrum. Methods Phys. Res. Sect. B Beam Interact. Mater. At.* **2013**, *312*, 110–117. [CrossRef]

32. Evseev, I.G.; Schelin, H.R.; Paschuk, S.A.; Milhoretto, E.; Setti, J.A.P.; Yevseyeva, O.; de Assis, J.T.; Hormaza, J.M.; Díaz, K.S.; Lopes, R.T. Comparison of SRIM, MCNPX and GEANT simulations with experimental data for thick Al absorbers. *Appl. Radiat. Isot.* **2010**, *68*, 948–950. [CrossRef] [PubMed]

33. Palaniyappan, S.; Huang, C.; Gautier, D.C.; Hamilton, C.E.; Santiago, M.A.; Kreuzer, C.; Sefkow, A.B.; Shah, R.C.; Fernández, J.C. Efficient quasi-monoenergetic ion beams from laser-driven relativistic plasmas. *Nat. Commun.* **2015**, *6*, 10170. [CrossRef] [PubMed]

34. Fernández, J.C.; Cort Gautier, D.; Huang, C.; Palaniyappan, S.; Albright, B.J.; Bang, W.; Dyer, G.; Favalli, A.; Hunter, J.F.; Mendez, J.; et al. Laser-plasmas in the relativistic-transparency regime: Science and applications. *Phys. Plasmas* **2017**, *24*, 056702. [CrossRef] [PubMed]

35. Bang, W.; Albright, B.J.; Bradley, P.A.; Gautier, D.C.; Palaniyappan, S.; Vold, E.L.; Cordoba, M.A.S.; Hamilton, C.E.; Fernández, J.C. Visualization of expanding warm dense gold and diamond heated rapidly by laser-generated ion beams. *Sci. Rep.* **2015**, *5*, 14318. [CrossRef] [PubMed]

36. Bang, W.; Albright, B.J.; Bradley, P.A.; Vold, E.L.; Boettger, J.C.; Fernández, J.C. Linear dependence of surface expansion speed on initial plasma temperature in warm dense matter. *Sci. Rep.* **2016**, *6*, 29441. [CrossRef]

37. Jung, D.; Hörlein, R.; Kiefer, D.; Letzring, S.; Gautier, D.C.; Schramm, U.; Hübsch, C.; Öhm, R.; Albright, B.J.; Fernandez, J.C.; et al. Development of a high resolution and high dispersion Thomson parabola. *Rev. Sci. Instrum.* **2011**, *82*, 013306. [CrossRef]

38. Schiwietz, G.; Grande, P.L. Improved charge-state formulas. *Nucl. Instrum. Methods Phys. Res. Sect. B Beam Interact. Mater. At.* **2001**, *175–177*, 125–131. [CrossRef]

39. Betz, H.-D. Charge States and Charge-Changing Cross Sections of Fast Heavy Ions Penetrating Through Gaseous and Solid Media. *Rev. Mod. Phys.* **1972**, *44*, 465–539. [CrossRef]

40. Ohuchi, H.; Yamadera, A. Dependence of fading patterns of photo-stimulated luminescence from imaging plates on radiation, energy, and image reader. *Nucl. Instrum. Methods Phys. Res. Sect. A Accel. Spectrometers Detect. Assoc. Equip.* **2002**, *490*, 573–582. [CrossRef]